

Article

# Long-Term Analysis of Sea Ice Drift in the Western Ross Sea, Antarctica, at High and Low Spatial Resolution

Usama Farooq <sup>1,\*</sup> , Wolfgang Rack <sup>1</sup> , Adrian McDonald <sup>1,2</sup> and Stephen Howell <sup>3</sup> <sup>1</sup> Gateway Antarctica, University of Canterbury, Christchurch 8140, New Zealand;

wolfgang.rack@canterbury.ac.nz (W.R.); adrian.mcdonald@canterbury.ac.nz (A.M.)

<sup>2</sup> School of Physical and Chemical Sciences, University of Canterbury, Christchurch 8140, New Zealand<sup>3</sup> Climate Research Division, Environment and Climate Change Canada, Toronto, ON, Canada; stephen.howell@canada.ca

\* Correspondence: usama.farooq@pg.canterbury.ac.nz

Received: 9 March 2020; Accepted: 26 April 2020; Published: 29 April 2020



**Abstract:** The Ross Sea region, including three main polynya areas in McMurdo Sound, Terra Nova Bay, and in front of the Ross Ice Shelf, has experienced a significant increase in sea ice extent in the first four decades of satellite observations. Here, we use Co-Registration of Optically Sensed Images and Correlation (COSI-Corr) to estimate 894 high-resolution sea ice motion fields of the Western Ross Sea in order to explore ice-atmosphere interactions based on sequential high-resolution Advanced Synthetic Aperture Radar (ASAR) images from the Envisat satellite acquired between 2002–2012. Validation of output motion vectors with manually drawn vectors for 24 image pairs show Pearson correlation coefficients of  $0.92 \pm 0.09$  with a mean deviation in direction of  $-3.17 \pm 6.48$  degrees. The high-resolution vectors were also validated against the Environment and Climate Change Canada sea ice motion tracking algorithm, resulting in correlation coefficients of  $0.84 \pm 0.20$  and the mean deviation in the direction of  $-0.04 \pm 17.39$  degrees. A total of 480 one-day separated velocity vector fields have been compared to an available NSIDC low-resolution sea ice motion vector product, showing much lower correlations and high directional differences. The high-resolution product is able to better identify short-term and spatial variations, whereas the low-resolution product underestimates the actual sea ice velocities by 47% in this important near-coastal region. The large-scale pattern of sea ice drift over the full time period is similar in both products. Improved image coverage is still desired to capture drift variations shorter than 24 h.

**Keywords:** sea ice; motion tracking; Envisat ASAR; Polar Pathfinder; NSIDC; Western Ross Sea; Synthetic Aperture Radar; COSI-Corr

## 1. Introduction

Sea ice thermodynamic and dynamic processes play an important role in the global climate as they significantly influence the Earth's energy balance and the freshwater flux [1]. Sea ice drift is a key driver of spatio-temporal variations in sea ice concentration and thickness. It is also a driver of roughness, surface albedo, moisture, and heat fluxes between the ocean and atmosphere, the freshwater budget, and the sea ice melt and growth rates [2,3]. Furthermore, for an accurate representation of sea ice in climate models, realistic parameterisation of the sea ice motion and deformation rates are required [4]. The drift of sea ice is primarily forced by winds and ocean currents and is an essential element in the dynamics of the polar oceans. In the Southern ocean, an overall increasing trend is observed in the sea ice extent over the last few decades with a significant expansion in the Ross Sea region ice, though the last few years potentially show signs of a reversing pattern [5]. The mechanisms

of this change are still uncertain. This is possibly driven by polynya processes in a few key areas. Coastal polynyas as a result of off-shore winds are areas that drive sea ice production and related processes and have likely contributed to a positive trend in sea ice extent and possibly mass in the Ross Sea [6,7]. The sea ice drift observations in polynya regions are extremely important to understand the sea ice formation and export mechanism. Winds over the Ross Sea have considerably strengthened in recent decades, possibly owing to a combination of natural variability [8,9], stratospheric ozone depletion concentrations, and changes in greenhouse gases [10].

Due to the vast area of the Antarctic sea ice cover and the timescale over which such investigations are required, satellite data provide the only feasible mechanism for large scale assessment of sea ice motion. Sea ice motion from consecutive satellite images can be estimated using Synthetic Aperture Radar (SAR) imagery (with C-band being the most common). SAR sensors provide imagery in various frequency bands with a high spatial resolution down to one meter and can be used in the presence of clouds and during the absence of visible light, both of which are considerable restrictions in the polar regions. Sea ice drift is estimated by comparing consecutive satellite images using one of the following methods: optical flow [11,12], pattern-matching [13], or feature tracking [14]. Authors of [15,16] developed a feature- and area-based technique for consecutive SAR scenes to calculate sea ice displacement of the entire Arctic Basin. Thomas et al. [17] introduced a comprehensive high-resolution sea ice drift algorithm for ERS-1 SAR images based on pattern-matching (phase-correlation and normalized cross-correlation), allowing motion calculation at 400 m pixel resolution. This phase-correlation method is faster than area-based techniques and is also able to identify rotational effects. The same modified approach was applied to Envisat advanced synthetic aperture radar (ASAR) data [18], which is derived of the sea ice motion field at 300 m resolution. Thomas et al. [19] modified the algorithm to calculate the sea ice motion close to the discontinuous regions in the Arctic. Komarov et al. [20] used the pattern matching technique for dual-polarization (HH and HV) SAR imagery and showed that images in HV polarization are preferred under certain conditions. Berg et al. [21] combines the phase-correlation method with feature tracking methods to form a hybrid algorithm, and shows that this can capture rotation as well as large-scale motion. Muckenhuber et al. [22] provided an open-source sea ice drift algorithm using the feature tracking technique and combined this with a pattern-matching scheme in later work [23], while [24] also used the same combination of feature tracking and pattern matching to calculate the sea ice drift in the Arctic. Most studies on high-resolution sea ice drift vectors are available for the Arctic, which is why the understanding of sea ice kinematics and its dynamics is much less developed for the Southern Ocean. The Antarctic sea ice is more difficult to track with commonly used SAR sensors because the younger and more homogeneous ice shows lower backscattering, less contrast, and high temporal variability [25]. In addition to this, other complicating factors include higher sea ice drift velocities, surface flooding, and snow accumulation, which make it altogether challenging to track prominent features in the sequential images.

However, low-resolution sea ice motion products are available for the whole Antarctic region. The Polar Pathfinder daily 25 km Equal Area Scalable Earth Grid (EASE-grid) sea ice motion vectors, version 4, of the National Snow and Ice Data Center (NSIDC), provide long term data from 1978 to present and were used in this study [26]. The advantages of these data are that they are available as a daily product on a regular grid with error variance and have Antarctic-wide spatial coverage. These low-resolution data are extensively utilized for parameter estimation in models, data assimilation, and validation of coupled ocean-sea ice models, together with other sea ice products like concentration and thickness [27]. For these applications, it is important to calculate the uncertainties in sea ice motion products. Hwang et al. [28] compared the six available sea ice motion products (three low-resolution and three medium-resolution) with the drifting buoy data in the Arctic and discussed the error distributions. Sumata et al. [27] compared the estimates of uncertainties in low-resolution products for the Arctic. For the Arctic monthly mean sea ice drift [29], produced time-varying uncertainty maps of low-resolution products with respect to high-resolution data sets, by applying an empirical

function. In [30], it was shown that for different products, the error statistics either depend on sea ice speed or on sea ice concentration, or on both, and also differ seasonally. Szanyi et al. [31] showed persistent artefacts in the NSIDC sea ice vectors for the Arctic due to the small scale drifting buoy data assimilation in satellite-derived sea ice vectors, which has been corrected in version 3. Previous Antarctic studies from the Weddell Sea and the Indian Ocean sector showed that sea ice motion derived from low-resolution satellite data underestimated sea ice motion by about 40% when compared to buoy data [32,33]; therefore, there is considerable need for high spatial resolution estimates.

In this paper, sea ice kinematics is derived based on repeat-pass, high-resolution SAR data for the western Ross Sea. Inter-comparisons over a time period of 10 years are made with available low-resolution products and by manual validation. Making use of the COSI-Corr software [34], we calculate high-resolution sea ice drift estimates and evaluate the applicability and shortcomings. The results are validated from manually drawn vectors and the performance is evaluated against the Environment and Climate Change Canada sea ice motion tracking algorithm. Conclusions are drawn in view of the complex sea ice deformation observed in the Western Ross Sea and potential limitations are assessed.

## 2. Study Area and Data

Our investigation area is the Western Ross Sea, including the three prominent polynyas: the Ross Sea Polynya (RSP), Terra Nova Bay Polynya (TNBP), and McMurdo Sound Polynya (MSP) (Figure 1). Antarctic-wide sea ice motion vectors derived from NSIDC for week 42 of 2011 are shown for the whole of Antarctica in Figure 1a. Figure 1b shows a blown-up image of the region of interest, which covers a total area of around 200,000 km<sup>2</sup>. Given that the prevailing wind and ice dynamics are not uniform across the study region, and that areas adjacent to Victoria Land are dominated by fast ice along the coastline, the area of investigation was split into two regions identified in Figure 1b: (i) RSP (region-1), and (ii) MSP and TNBP (region-2).

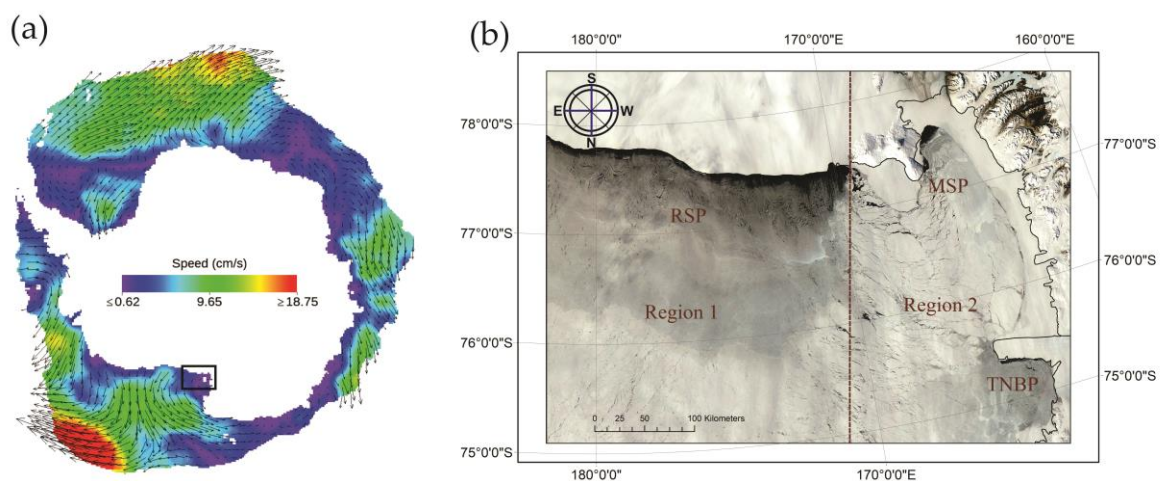


**Figure 1.** (a) Antarctic-wide mean National Snow and Ice Data Center (NSIDC) sea ice drift vectors for week 42 of 2011 (box indicates study area). (b) Moderate Resolution Imaging Spectroradiometer (MODIS) image (27 October 2011) of the study region in the western Ross Sea showing three prominent polynyas: the Ross Sea Polynya (RSP), Terra Nova Bay Polynya (TNBP), and McMurdo Sound Polynya (MSP).

### 2.1. ASAR High-Resolution Radar Image Data

Envisat ASAR wide swath (WS) images (C-band; HH polarization) in ScanSAR mode were analysed for the satellite operational years 2002–2012 during the winter period of April–October, which is when the study area shows near-complete sea ice coverage. WS products are acquired at a swath width of 400 km at a nominal resolution of 150 m, and the GRD (Ground Range Detected)

product is gridded at a 75 m pixel raster. Data in radar geometry were projected into the same polar-stereographic coordinate system as the NSIDC product (see below). The acquisition time was around 18:00 UTC (varying between 15:00–20:00 UTC). These data were found to be suitable for sea ice motion detection due to their comparatively large spatial and temporal coverage. As shown in Table 1, for our investigation area, a total of 2829 images with full or partial coverage of the study area over the 10-year period examined were assessed. Out of the 2829 satellite images originally available, we selected 1513 images with at least 50% coverage of the study area defined in Figure 1a for further analysis. Overall, this resulted in 894 velocity fields, with 480 having a 1-day time separation.

**Table 1.** Monthly and annual distribution of Envisat advanced synthetic aperture radar (ASAR) wide swath images acquired on a variety of ascending and descending orbits in the study area.

Months	2002	2003	2004	2005	2006	2007	2008	2009	2010	2011	2012
April		8	8	18	16	14	6	11	12	27	5
May		2	11	43	20	17	5	13	9	10	
June		8	3	31	19	14	5	9	12	24	
July		8	-	30	20	11	10	8	10	18	
August	11	9	8	28	20	8	13	6	10	17	
September	8	10	16	31	9	6	11	4	7	17	
October	13	3	11	27	22	10	13	13	11	27	
Annual Total	32	48	57	208	126	80	63	64	71	140	5
Grand Total						894					

The precise geo-referencing of Envisat ASAR imagery is one of the most important factors for sea ice motion calculations. Data were received in ground range detected (GRD) format and calibrated by applying calibration constants provided in the ESA product. The images were also down-sampled from 75 m to 150 m for speckle reduction and converted into a polar-stereographic projection using the GAMMA Remote Sensing software package. Most of the observed backscattering coefficient ( $\sigma^0$ ) values were between 0 and  $-25$  dB, and were well within the expected range for ASAR wide swath mode data [35]. The SAR data were scaled to 8-bit using a power-law scaling with an exponent of 0.35 in order to keep the data volume low whilst also representing the dynamic range and the radiometric accuracy of the sensor [35].

## 2.2. NSIDC Sea Ice Motion Vector

For the low-resolution sea ice motion, Polar Pathfinder Daily 25 km EASE-Grid Sea Ice Motion Vectors, version 4 (provided by the NSIDC), were used. NSIDC provides daily gridded sea ice motion vectors on a 25 km grid from November 1978 to the present. The data are on a regular South Polar-stereographic grid with vector components in the direction of the easting and northing coordinates in cm/s, and a third variable describes the square root of the estimated error variance. The vectors are defined on EASE-Grid. In contrast to the Arctic, where sea ice motion is calculated using multiple instruments, buoys, and wind data sets, for the Southern Ocean, the motion is computed only from satellite data [26]. We used the NSIDC data for comparison with the Envisat data from 17 August 2002 to 7 April 2012.

## 3. Methods

For our study, we first estimated the sea ice motion using the COSI-Corr (Co-Registration of Optically Sensed Images and Correlation) software package (an add-on module in ENVI classic software). This software was originally developed for the evaluation of coseismic displacement fields [34]. Scherler et al. [36] found COSI-Corr to be useful for glaciological applications to derive the glacier velocities. Here, we evaluate the potential and limitations of this software for sea ice motion detection and compare the high-resolution drift vectors to a standard 25 km motion product.

### 3.1. Drift Vector Calculations

We calculated sea ice motion vectors from consecutive high-resolution Envisat image pairs in centimetres per second using the frequency correlator in the COSI-Corr software. Key elements of the frequency correlator are outlined here, but a detailed description can be found in [34]. Based on the Fourier transform (FT) of the images, the relative displacements between image patches are calculated by evaluating the correlations between the images from a multi-pixel to sub-pixel scale. A Hanning window is used for the image patches to reduce the FT windowing artefacts, and high frequencies are masked by filtering to improve the correlation quality. A sliding window is used to scan the images to calculate the correlation fields to obtain the motion components in the x- and y-direction and the corresponding Signal to Noise Ratio (SNR). The frequency correlation is a two-step process. In the first step, the coarse displacement is calculated between two images by setting up an initial window size (IWS). After this coarse displacement is estimated, a final smaller window size (FWS) is used to estimate the accurate subpixel displacement. In total, there are five variable settings that are controllable in the COSI-Corr software; these are: IWS, FWS, Step distance in x- and y-direction, Robustness Iteration number (RI), and Mask Threshold (MT). We carried out a robustness test by changing only one variable and leaving the remaining variables constant and found that results are highly sensitive to IWS. The reason for this sensitivity is that large displacements can only be observed by making the IWS sufficiently large. For example, an IWS of 256 in the frequency correlator setting allows by default only a 128 search range in each direction [37] and, therefore, restricts the maximum detectable displacement to 19.2 km for our 150 m pixel resolution image. As in the event of polynya openings, the maximum ice displacement was found to be around 30 km in 24 h in our study region based on a visual assessment. Estimating maximum one-day sea ice drift, we used for our analysis 512, 64, 4, and 0.9 for IWS, FWS, RI, and MT, respectively. The resulting COSI-Corr motion vectors were saved as vector components with a measure of the Signal to Noise Ratio (SNR) varying between 0–1. We masked the land area and also removed large outlying vectors that were observed on the edges between two images. In the quality control step, we discarded all the values that had an SNR value of less than 0.95.

For all the selected image pairs, we also used high-resolution vectors calculated by the Environment and Climate Change Canada sea ice motion tracking algorithm (hereafter referred to as ECCC), which is fully described and based on [20]. Briefly, this algorithm uses the phase-correlation and cross-correlation combination to capture the rotational and translational sea ice movement. It was found to have a root-mean-square error of 0.43 km/day [20] between the ice drifting beacon trajectories and the SAR-derived sea ice motion vectors. The ECCC algorithm has been widely used for sea ice applications in the Arctic (e.g., [38,39]).

### 3.2. Validation of COSI-Corr Motion Vectors

A common method to validate satellite-derived sea ice motion vectors is to use continuous sea ice drift buoys (e.g., [40]). However, no buoy data are available for our study area and, therefore, the sea ice motion vectors had to be validated with manually drawn vectors. Start and end points of clearly identifiable ice floes were used to draw displacement vectors in ArcGIS. For the validation, we selected October 2011 as a month with representative sea ice extent and good satellite data coverage in terms of availability of images for a single month over the entire study area. A large variety of possible drift patterns were also observed in October 2011 (see examples in Figure 4), and the radar backscattering signatures in other months were found to be very similar to this validation period. We found a total of 24 image pairs and around 50 vectors per image pair were derived manually. Scatter plots were used to examine the agreement between manual and COSI-Corr displacement magnitudes, and the Pearson correlation coefficient was evaluated. The directional differences were quantified using the deviation between the two vectors. Positive angle values were assigned if the manual vector was to the right of the Envisat vector; otherwise, it was considered to be a negative deviation. The standard deviation was also calculated. Furthermore, the ECCC vectors are also compared with manually drawn vectors

and based on the high correlation (discuss in result section) shown later, which is used as a benchmark for the validation of the COSI-Corr vectors for all the years (2002–2012).

### 3.3. Comparison Between High-Resolution and Low-Resolution Data

For comparison with the NSIDC data set, we downsampled the high-resolution vectors to  $25 \times 25$  km pixel resolution. The image section for our analysis is shown in Figure 1b, which has a length and width of  $525 \text{ km} \times 375 \text{ km}$  corresponding to  $3500 \times 2500$  pixels at our nominal pixel size of 150 m. The NSIDC sea ice grids come at 25 km resolution, corresponding to  $21 \times 15$  pixels for this image section.

We used the  $10 \times 10$  step size for deriving COSI-Corr vectors, so our final correlation image is downsampled by a factor of 10 to 1500 m pixel resolution ( $350 \times 250$  pixels). We inserted 7 blank rows and 5 blank columns ( $357 \times 255$  pixels) at the margins so that they can be divided by 17 (so that the output is  $21 \times 15$  pixels). The margins were subsequently masked for further processing. The COSI-Corr result also has no data values when there are no data or the correlation value between the two images is below the validity threshold. Therefore, we averaged  $17 \times 17$  pixels by excluding pixels with no data. To minimize a bias in the down-sampling, we averaged only those pixel templates that had more than 60% of data values. For example, if the number of populated vectors was 50 out of 100 pixels ( $10 \times 10$ ), then the average might differ from the pixel where more or all pixels have values, due to the large variation in the sea ice motion vectors. These steps gave us a smooth and filtered sea ice drift field. Sea ice vectors are co-located for comparison using the nearest neighbour method. We drew the scatter plots with the linear fit and calculated the correlation coefficient for the image pairs with one-day separation, this reduced the number of usable vector fields to 480. Scatterplots as shown in Figure 6a were evaluated if more than 5 corresponding data points were available in Envisat data. The overall comparison methodology is detailed graphically in Figure 2.

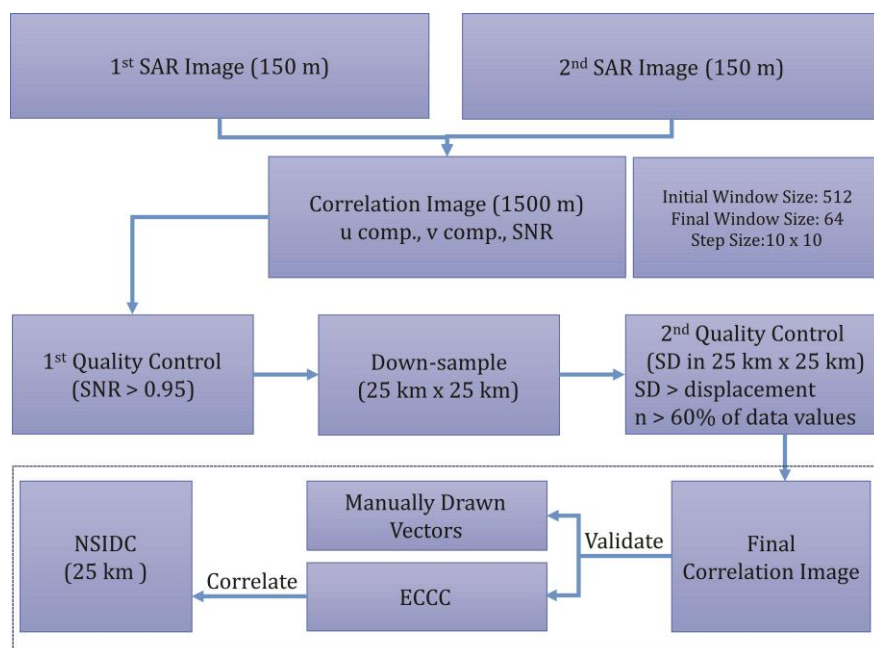


**Figure 2.** Flow diagram explaining the applied analysis method.

Finally, the NSIDC data were also used to describe the average speed (in cm/s) and flow direction (in degrees) over the study area from 2002–2012. The same procedure was adopted for the high-resolution data, and average speed was calculated for the available image pairs for region-1 and region-2. The results are presented in Section 4.3.

#### 4. Results

We analysed the Envisat data for the years 2002–2012 during the winter period April–October when the area shows near-complete sea ice coverage apart from regular Polynya events (Figure 2a in [7]). Probability Density Functions (PDFs) were calculated for a bin size of 0.5 cm/s for region-1 and region-2 for all the available image pairs from 2002–2012 (Figure 3). We also divided the data into two seasons from 01 April–15 July and from 16 July–31 October. The Envisat derived vectors are downsampled to the resolution of the NSIDC grid for the calculation of the PDFs. Based on the results of the Kolmogorov–Smirnov test, it is observed that the distributions are significantly similar for both seasons.

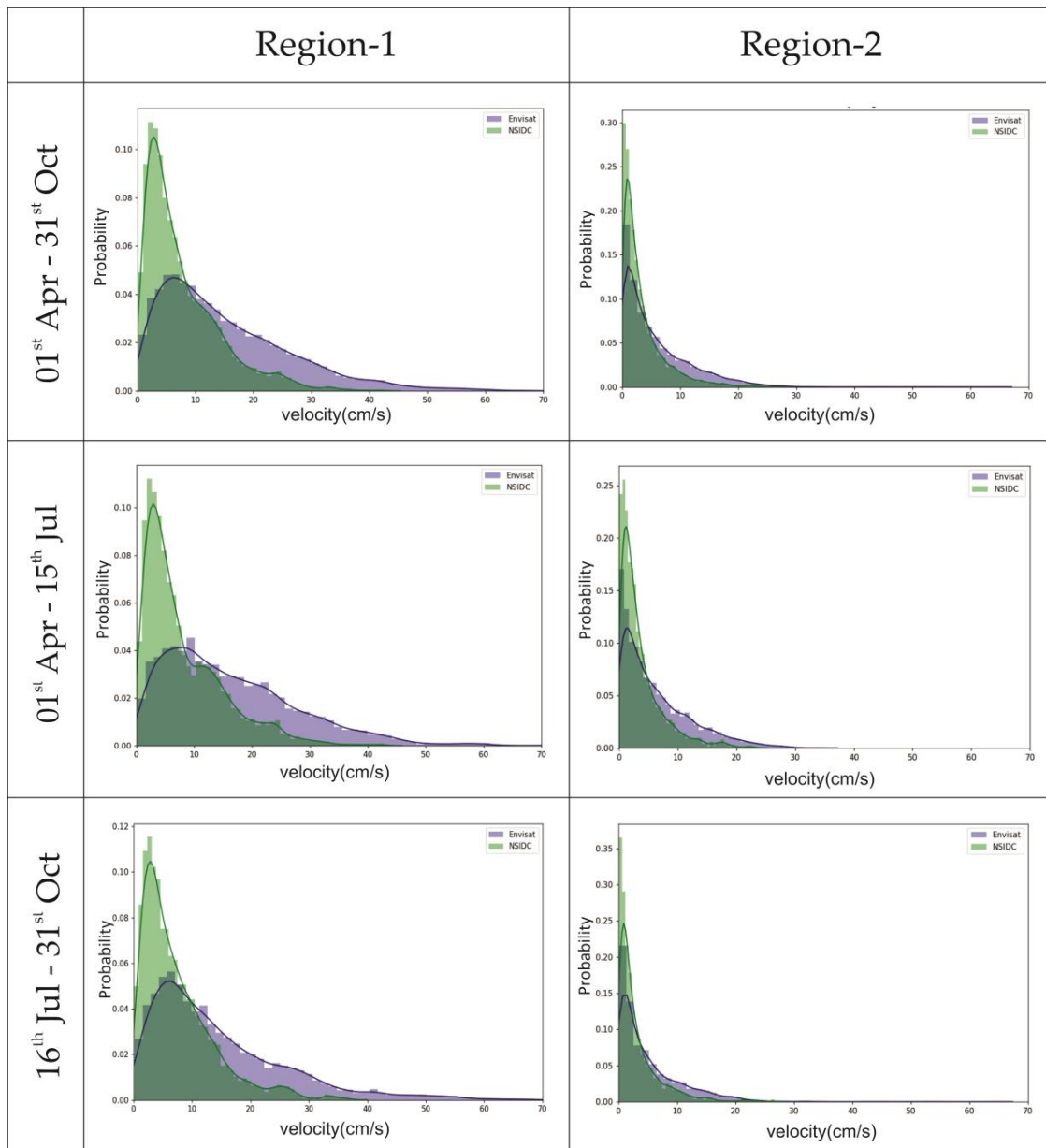


**Figure 3.** Probability density functions (velocity bin size at 0.5 cm/s) for all the available data from 2002–2012 for region-1 and region-2 for two seasonal periods. Data are divided into two seasons from 01 April–15 July and 16 July–31 October. The solid lines represent running means.

Examples of consecutive Envisat SAR images used in our analysis are shown in Figure 4 with overlaid drift vectors from high- and low-resolution products. These sample images show the variation

in the sea ice motion and different possible directions in which the sea ice drift in the Western Ross Sea region. Figures 5 and 6 show a comparison of Envisat automatic and manual vectors, and Envisat and NSIDC sea ice drift, respectively. Tables 2 and 3 represent the mean correlation coefficient in magnitude and direction.

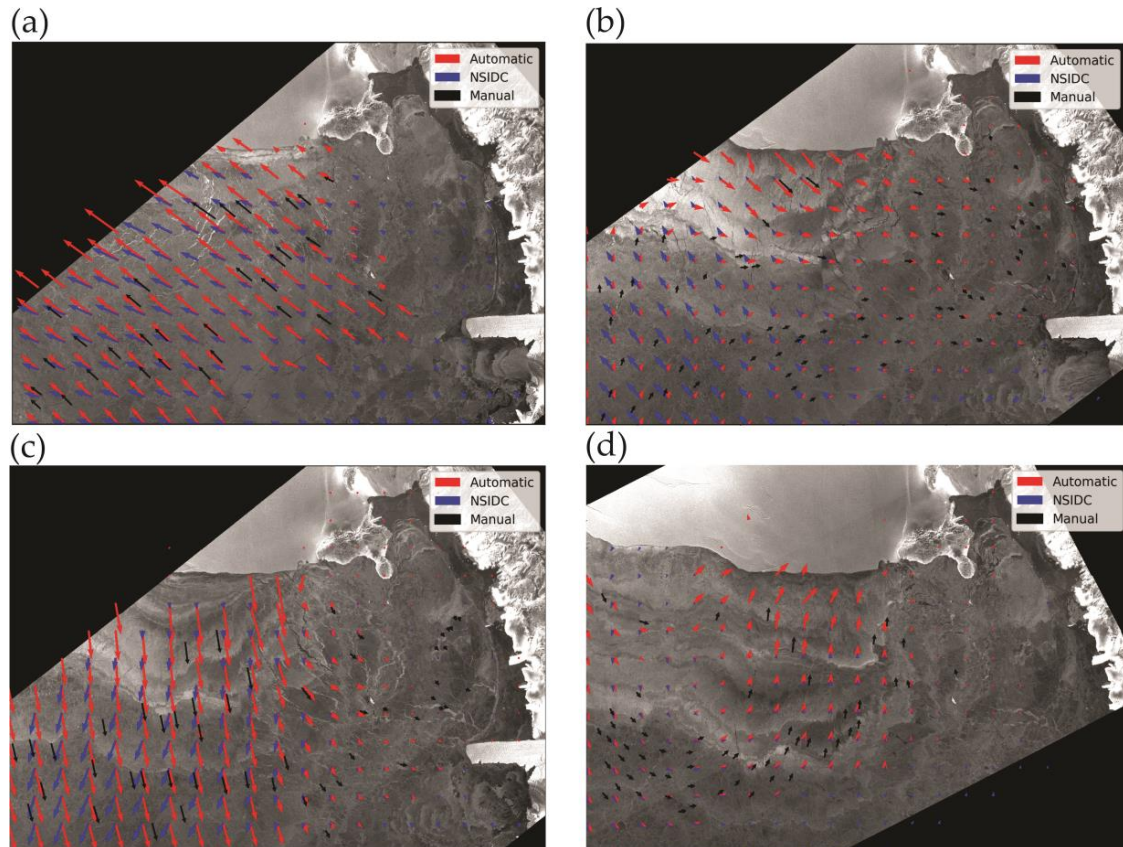


**Figure 4.** Displacement vectors of 25 km grid resolution obtained from different methods are plotted on Envisat images. (a) Vectors for 01–02 October 2011, (b) 16–17 October 2011, (c) 24–25 October 2011, and (d) 28–29 October 2011.

#### 4.1. Validation Results: Envisat Manual Versus Automatic Vector

For validation, we used October 2011 as a sample month because it is when sea ice concentration is high and a sufficiently large number of image pairs are available (24 image pairs) for comparison. Displacement vectors were manually drawn for sequential image pairs and the Pearson correlation coefficients were calculated. Vectors were co-located using the nearest neighbour method for comparison. The high-resolution drift vectors were automatically derived by using two techniques (i) COSI-Corr and (ii) ECCC. We compared the ECCC with the manually drawn vectors and found the correlation coefficient in speed ( $0.98 \pm 0.02$ ) and mean deviation in direction ( $-0.79 \pm 2.00$ ) degrees. This implies that the ECCC algorithm has high accuracy for visually stable and identifiable features. However, we also validated COSI-Corr vectors with manual vectors but, as the manual vectors were only drawn for one month, we also compared COSI-Corr vectors with ECCC for the whole data set (total 894 image pairs from 01 Apr–31 October of each year from 2002–2012). The results are summarized in Table 2 with an example of 10–11 October 2011 in Figure 5. The mean correlation coefficient ( $R$ ) is found to be  $0.84 \pm 0.20$  for the speed and the mean deviation in angles is  $-0.04 \pm 17.39$  deg.

**Table 2.** Validation parameters with standard deviations of COSI-Corr vectors from manual and Environment and Climate Change Canada (ECCC) automatic drift vectors with the deviation in the direction.

Algorithm	Displacement (km)				Image Pairs	Directional Difference (deg)
	Slope	Intercept	R	RMSE		
ECCC vs. manual	$1.00 \pm 0.05$	$-0.02 \pm 0.38$	$0.98 \pm 0.02$	$0.73 \pm 0.41$	24	$-0.79 \pm 2.00$
COSI-Corr vs. manual	$1.05 \pm 0.52$	$-0.66 \pm 2.10$	$0.92 \pm 0.09$	$1.02 \pm 0.82$	24	$-3.17 \pm 6.48$
COSI-Corr vs. ECCC	$0.77 \pm 0.32$	$0.51 \pm 3.05$	$0.84 \pm 0.20$	$2.77 \pm 3.86$	894	$-0.04 \pm 17.39$

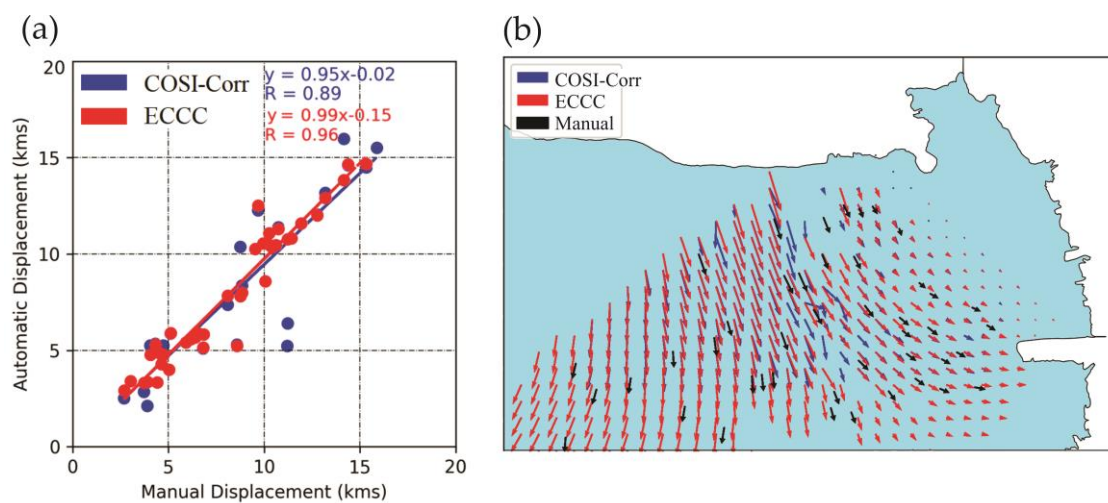


**Figure 5.** Sample validation procedure for the image pair of 10–11 October 2011. (a) Scatter plot for COSI-Corr and ECCC comparison with manual vectors. (b) Visual representation of vectors obtained from different techniques.

#### 4.2. Envisat Automatic Versus NSIDC Vectors

When comparing the high-resolution image data set to the low-resolution NSIDC data set, we downsampled the high-resolution images rather than interpolating them. We compared both COSI-Corr and ECCC with NSIDC data, but ECCC works for both low and high velocities and is more accurate, so here we reported the result of these vectors for comparison (details are described in the discussion in Section 6). We calculated the correlation coefficient and the difference between angles. Figure 6 shows a comparison example of the NSIDC sea ice motion vectors with the Envisat high-resolution image vectors. The speed was calculated for each grid point and the results were plotted as a scatter plot. For each image pair, the least square regression line was fitted. From this, gradient, intercept, Pearson correlation coefficient, and root mean square error (RMSE) were calculated. The angle deviation was also calculated at each grid point. The same procedure was repeated for all the image pairs, and the large-scale statistics are reported year-wise in Table 3.

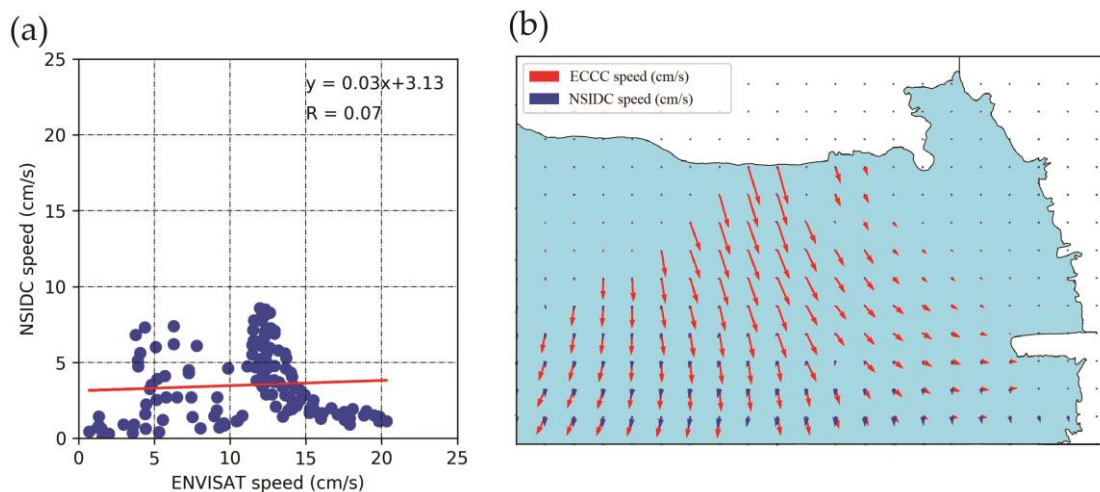
Based on the results shown in Figure 6, we further investigated the minimum and maximum velocities captured by both data sets to analyse the variations in the sea ice velocities. To further examine this, the range of velocity values for both the NSIDC and the Envisat data sets were compared for each region. For all study years, the range of NSIDC velocities were more often smaller than the range of Envisat: 90.11% of the time in region-1 and 92.42% of the time in region-2.

**Table 3.** Correlation coefficient (R) for drift velocity (cm/s) and deviation in drift direction (degrees) between Envisat images and NSIDC data: (a) region-1; (b) region-2.

<b>(a) Region-1—Speed (cm/s)</b>						
Year	Slope	Intercept	R	RMSE	Image Pairs	Directional Difference (deg)
2002	0.07 ± 0.45	4.20 ± 4.75	0.30 ± 0.48	6.68 ± 4.97	22	3.57 ± 42.13
2003	0.18 ± 0.35	5.10 ± 4.58	0.27 ± 0.53	13.29 ± 9.68	27	9.75 ± 20.69
2004	0.09 ± 0.29	3.83 ± 3.60	0.09 ± 0.47	10.91 ± 9.12	27	−9.61 ± 28.08
2005	0.15 ± 0.57	4.21 ± 7.79	0.20 ± 0.59	13.22 ± 10.75	101	−9.34 ± 37.74
2006	0.06 ± 0.33	7.17 ± 6.78	0.06 ± 0.51	11.84 ± 10.19	92	−1.38 ± 44.13
2007	0.09 ± 0.30	7.64 ± 6.83	0.14 ± 0.50	13.95 ± 10.41	40	5.11 ± 32.56
2008	0.13 ± 0.32	5.98 ± 5.69	0.19 ± 0.55	8.30 ± 7.26	23	−3.59 ± 29.86
2009	0.16 ± 0.38	6.65 ± 8.62	0.23 ± 0.50	12.22 ± 9.65	25	−6.52 ± 33.56
2010	0.27 ± 0.34	6.91 ± 7.32	0.33 ± 0.50	8.61 ± 5.87	16	−0.43 ± 26.39
2011	0.20 ± 0.47	7.05 ± 11.62	0.22 ± 0.51	9.39 ± 8.37	104	−2.18 ± 40.33
2012	−0.13 ± 0.17	7.03 ± 3.49	−0.20 ± 0.27	14.26 ± 5.15	4	−15.03 ± 8.55
Weighted Average	0.13	-	0.18	11.33	-	-

<b>(b) Region-2—Speed (cm/s)</b>						
Year	Slope	Intercept	R	RMSE	Image Pairs	Directional Difference (deg)
2002	0.22 ± 0.32	2.18 ± 3.88	0.41 ± 0.44	3.58 ± 3.06	22	−2.10 ± 47.65
2003	0.21 ± 0.23	2.04 ± 1.71	0.41 ± 0.48	4.10 ± 2.97	27	−3.34 ± 43.90
2004	0.13 ± 0.19	1.67 ± 1.86	0.37 ± 0.41	4.60 ± 4.04	27	−3.50 ± 54.06
2005	0.11 ± 0.30	2.91 ± 3.68	0.35 ± 0.42	6.32 ± 4.55	101	−9.52 ± 39.85
2006	0.23 ± 0.28	3.00 ± 3.75	0.45 ± 0.43	4.96 ± 3.18	92	4.92 ± 38.99
2007	0.12 ± 0.18	4.28 ± 3.98	0.32 ± 0.38	5.83 ± 3.52	40	11.30 ± 50.01
2008	0.29 ± 0.51	2.46 ± 3.25	0.48 ± 0.39	3.99 ± 2.80	23	14.48 ± 42.00
2009	0.21 ± 0.26	3.59 ± 4.79	0.41 ± 0.35	5.19 ± 4.12	25	−2.18 ± 56.15
2010	0.18 ± 0.12	2.50 ± 1.84	0.45 ± 0.27	5.55 ± 2.01	16	4.48 ± 31.61
2011	0.22 ± 0.43	2.96 ± 3.72	0.33 ± 0.41	4.72 ± 3.26	104	2.47 ± 45.92
2012	0.04 ± 0.07	1.78 ± 0.80	0.18 ± 0.51	11.84 ± 1.85	4	−7.74 ± 3.13
Weighted Average	0.18	-	0.38	5.18	-	-



**Figure 6.** Image pair of 10–11 October 2011 showing the captured variation. (a) Scatter plot with a least-square fit for low and high-resolution data set. (b) Graphic representation of vectors gathered from the Envisat and NSIDC data sets on a 25 km grid resolution.

### 4.3. Average Speed Comparison Over the Study Area

We also completed an average speed comparison by using a spatial average of the sea ice velocities for region-1 and region-2, but spatial averages were only calculated if grid points were available for both Envisat and NSIDC. A time series of the results for 2011 is shown in Figure 7, and the summary for all years is shown in Table 4. The Spearman rank correlation coefficients for all the image pairs of all years are found to be 0.55 and 0.53 for region-1 and region-2, respectively.

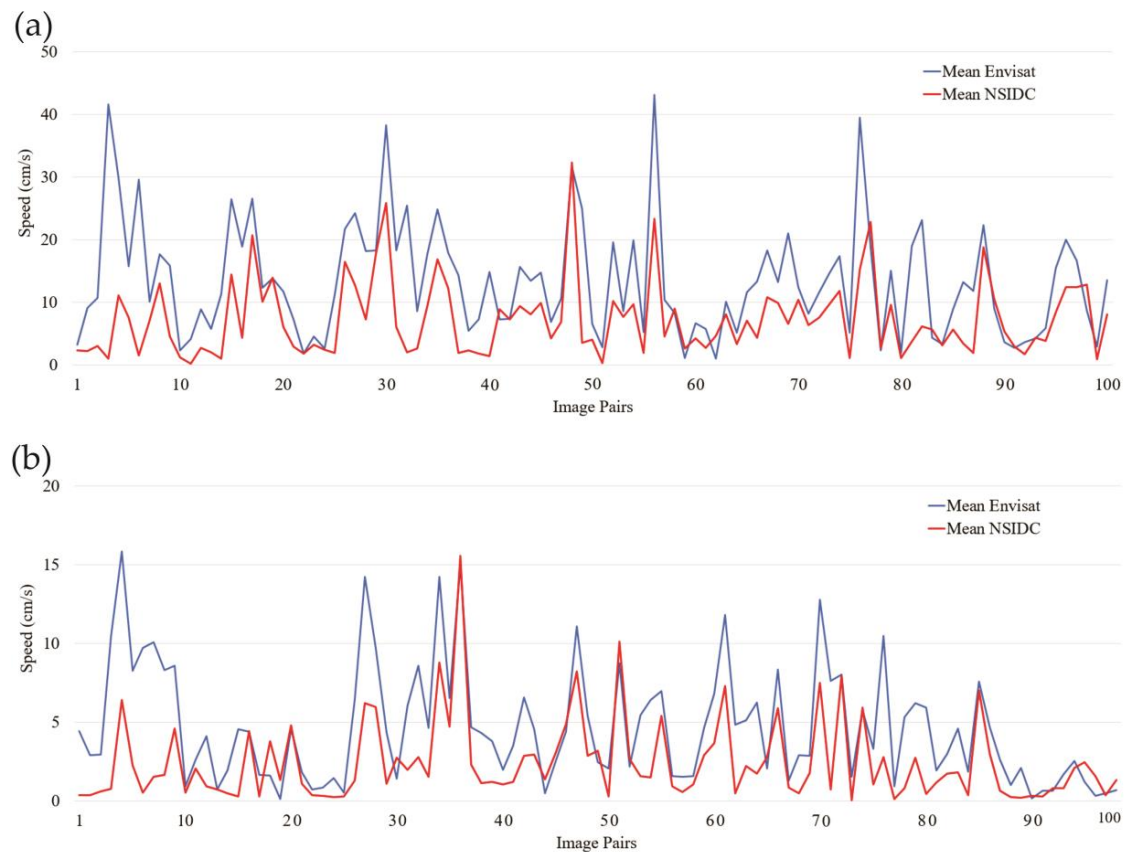


**Figure 7.** Graph showing average speed for low and high-resolution images for the available image pairs for the year 2011 over (a) region-1 and (b) region-2.

Furthermore, to examine the long term averages in sea ice motion, the velocities were divided into three categories based on the percentiles of sea ice speed: low (0–10 cm/s), medium (10–20 cm/s), and high (>20 cm/s) in region-1, and low velocities (0–5 cm/s), medium velocities (5–10 cm/s), and high velocities (>10 cm/s) in region-2. For the directional analysis, the directions were divided into four categories (East, West, North, and South). For example, here ‘North’ represents the direction in which the sea ice was drifting due to the winds coming from the Ross Ice Shelf (RIS). However, the sea ice was moving to the east due to the katabatic winds blowing from the Transantarctic Mountains and through Terra Nova Bay. Other directions were also assigned in a similar way (Figure 1). The directional bins for the sea ice roses in Figure 8 are represented in the same way as the overlaid sea ice motion vectors in the polar-stereographic coordinate system. Finally, the four directions categories were considered as  $\pm 45$  deg deviation from that cardinal direction. The results are summarized in Table 4 for the regions (1 and 2), and sea ice roses are shown in Figure 8. These results are discussed in detail in the next section.

**Table 4.** Distribution in percentage of sea ice velocities related to wind speed categories and direction  $\pm 45$  degrees from the cardinal direction from 2002–2012. (a) Envisat derived vectors for region-1. (b) NSIDC calculated sea ice motion for region-1. (c) Envisat derived vectors for region-2. (d) NSIDC calculated sea ice motion for region-2.

<b>(a) Envisat (Region-1)</b>				
Categories (cm/s)	Low (0–10)	Medium (10–20)	High (>20)	
S	6.07	0.22	0	6.29
W	6.07	5.17	0.45	11.7
N	17.3	24.27	24.04	65.6
E	9.66	5.17	1.57	16.4
	39.1	34.83	26.07	100
<b>(b) NSIDC (Region-1)</b>				
Categories (cm/s)	Low (0–10)	Medium (10–20)	High (>20)	
S	7.42	0	0	7.42
W	14.61	1.8	0	16.4
N	39.78	14.38	2.92	57.1
E	16.4	2.47	0.22	19.1
	78.2	18.65	3.15	100
<b>(c) Envisat (Region-2)</b>				
Categories (cm/s)	Low (0–5)	Medium (5–10)	High (>10)	
S	5.19	0.22	0	5.41
W	10.82	2.6	0.87	14.3
N	30.95	11.9	3.03	45.9
E	23.59	8.01	2.81	34.4
	70.56	22.73	6.71	100
<b>(d) NSIDC (Region-2)</b>				
Categories (cm/s)	Low (0–5)	Medium (5–10)	High (>10)	
S	7.36	0	0	7.36
W	8.23	1.08	0	9.31
N	49.13	6.49	1.95	57.6
E	24.68	1.08	0	25.8
	89.39	8.66	1.95	100

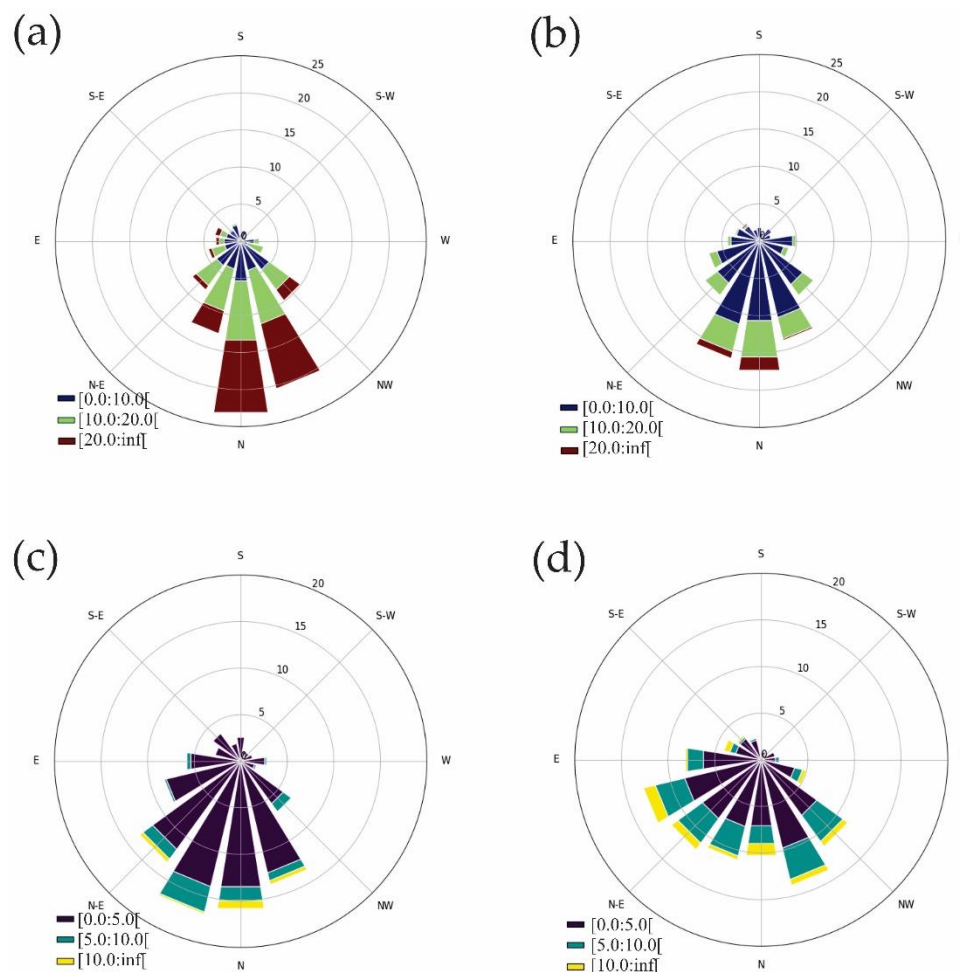


**Figure 8.** Sea ice drift roses from 2002–2012. (a) and (c) are derived from Envisat data set for region-1 and region-2, respectively, and (b) and (d) from NSIDC sea ice motion vectors for region-1 and region-2, respectively.

## 5. Discussion

Keeping in mind the variable sea ice conditions and dynamics, the sea ice drift is higher in the Ross Sea polynya region due to the stronger southerly winds. Off-shore winds blowing from the south across the western RIS are responsible for the regular opening of the Ross Sea polynya [7]. Compared to the Ross Sea polynya region, the McMurdo Sound polynya experiences a modified wind regime because of more complex geography. This area is adjacent to fast ice, and sea ice is often not freely drifting as shown in Figure 1. The area immediately north of Ross Island is a natural boundary, as it is protected from the dominant southerly winds [7]. In the opening of the TNBP sea, ice in the area is moving east, but the predominant winds along the coast change its bearing to the north-east in between polynya events [41]. Our analysis, therefore, confirmed that the study area can be divided into two regions experiencing significantly different sea ice dynamics related to differing wind forcings: RSP (region-1), and MSP and TNBP (region-2).

We made use of the available COSI-Corr software package to calculate the sea ice motion vectors. The quality of COSI-Corr vectors mainly depends upon three factors. Firstly, and most importantly, we must pick a suitable initial window size (IWS) to detect the maximum sea ice displacement. This is a critical limitation especially for the COSI-Corr algorithm, which was developed for relatively small displacements. The other tuning parameters do not result in significant differences in the calculated sea ice velocity fields. For instance, in our analysis, we chose an IWS of 512 pixels and, therefore, the maximum detectable displacement in the Euclidean space between consecutive images is 38.4 km.

Secondly, during periods of polynya formation, the young sea ice is highly deformable without any significant stable features, which normally does not allow us to find matching points even over very short periods of time. In a few cases, it was observed that in the event of polynya formation, up to half of the study area was open water; hence, only a few matching features are available in the study area. Finally, an important aspect dictating the COSI-Corr vector population is the image overlap area itself. If the images cover less than 50% of the overlapping area of the study region, then the outside 'no data' values make it increasingly difficult to find good quality matching points. Another consideration is the satellite image contrast, given that results shown here are based on Envisat WS images with relatively high SNR. In other study regions, or for example by using Envisat SAR images in GMM mode, results could be impacted by a low SNR. It is also observed that under the conditions mentioned above, the COSI-Corr algorithm is suitable for different ice conditions and seasons as well. The algorithm shows promising results with input parameters as discussed. The presented results of sea ice drift are in agreement with a study by Hollands et al. [42], who found that four error sources are linked to image data properties. These are the following: the homogenous regions of newly formed ice without any textural pattern, brightness changes in the images due to the polynyas, ice structures and similarity changes between image pairs (rotation, deformation, and melting), and at the borders as the floe enter/left the study area.

The accuracy of COSI-Corr was evaluated with the manually drawn vectors, and the sources of error were mainly dependent upon the manual picking of matched key-points in two consecutive images. The errors also depend on the distance between the manual and COSI-Corr vector found by the nearest neighbour method. Overall, there were four error sources: locational geo-referencing error, manual picking of key-point and vector, algorithm error, and vector co-location error. For example, in the error budget, if the images with an error of two pixels are 24 h apart with 150 m pixel resolution, they can generate an error of  $\pm 0.35$  cm/s in the resultant vector field. Results depict a high correlation between automatic and manually drawn vectors with appropriate representation of direction. The COSI-Corr vector works for a maximum drift speed of 45 cm/s, while ECCO shows that it works for all velocity ranges from low to high with high accuracy, as indicated in Table 2.

The correlation of the Envisat data set with NSIDC sea ice motion varies with the image pair. For this comparison, the source of error includes the co-location error. Furthermore, there might be another source of uncertainty in the comparison due to the acquisition time of the images, since the limited number of high-resolution data sets are always acquired around 18:00 UTC. However, low-resolution data are acquired at varying times of the day. When comparing the Envisat data with the NSIDC data set, no strong correlation was found between their speeds and directions. Table 3 outlines for the 10-year data set that the correlation coefficients (R) are 0.18 and 0.38 for region-1 and region-2, respectively. As shown in Figure 6, most of the least square linear fit lines are parallel to the Envisat velocity axis. This demonstrates that deformation patterns in the study area are much smaller than the grid spacing in the NSIDC data. Therefore, the lower spatial resolution of the NSIDC vector set is unable to capture the fine-scale spatial variability observed by the SAR data. The range of the velocity values is calculated by subtracting the maximum velocity from the minimum velocity for each deformation field of the NSIDC and Envisat data set, and the corresponding line graphs were analysed. The same finding is also reflected in the range of velocity values for all the image pairs. It shows the range of drift velocities calculated from the NSIDC data set are more often lower than the high-resolution data set for both regions (90.11% and 92.42% of the time for region-1 and 2, respectively). Table 3a,b also depicts that the mean deviation in that direction is also high. Previous studies have described that the temporal and spatial uncertainty relies on four main sources of error in openly available sea ice drift products for the Arctic: algorithm used for sea ice tracking, interpolation method, satellite input data, and temporal and spatial scales [27]. For our analysis, the lower spatial variability in the NSIDC data set might be due to the unavailability of input satellite data, which results in the interpolation or extrapolation of the data set to populate all the grid points in the study area. Researchers in [32] compared the low-resolution satellite-derived sea ice motion with drifting buoys,

and also found a very low correlation coefficient of 0.15 in speed for East Antarctica from 1985 to 1997. Buoy data represent the motion of individual floes (similar to the derived high-resolution sea ice motion in this study), whereas the low-resolution sea ice motion vectors represent the drift of surface patterns within a much larger grid-cell.

In addition to the observations of spatial variation of sea ice motion, the average speed over both regions was also examined. Based on the comparison of average speed over the study area, Figure 7 reveals that NSIDC mean velocities are underestimated around 47.37% for the entire study area in comparison to the high-resolution data set. Researchers in [33] compared the low-resolution satellite-derived sea ice motion with the drifting buoy data for the Weddell sea from 1989 to 2005, and also found that NSIDC drift was underestimated by 34.5% in comparison to the mean drift velocity calculated from drifting buoys. Furthermore, [32] showed for East Antarctica from 1985 to 1997 that the typically satellite-derived sea ice motion underestimated 40% or less of the buoys derived ice velocity. This indicates that the shortcoming in previous studies are related to the spatial scale of the input data and can be overcome by using high-resolution SAR images. The comparison shows that a very high sea ice motion towards the Drygalski ice tongue in the low-resolution image is not observed when using high-resolution satellite images and some NSIDC images are not capturing the actual rotation as detected in Envisat data. This shows that when using low-resolution data for a short period of one day, it is important to consider the overall statistics of sea ice in the Western Ross Sea. Otherwise, results might be biased for the velocity estimates. Due to the availability of restricted image pairs, it is difficult to determine under which conditions and circumstances NSIDC vectors show the same estimates as the velocity magnitude and direction obtained from high-resolution satellite data set. Our study shows that the high-resolution SAR images have the ability to estimate the small and fine-scale movements of ice floes, but they also indicate a very interesting fact about the NSIDC data set, which is that it has the ability to capture the average speed trend over the study area. We can observe that on those occasions when the Envisat derived speed is maximum, the NSIDC sea ice motion is also showing a peak. The Spearman rank correlation coefficient is found to be around 0.5 for the study area. Therefore, for the NSIDC data set, the NSIDC average speed analysis is more appropriate than the NSIDC pixel by pixel analysis and gives a better estimation of the actual speed over the study area.

Another interesting aspect from these images is that we can perform a more detailed directional analysis to examine the most dominating speed and direction in which sea ice is typically moving. To investigate the overall velocity statistics, sea ice speed has been divided into three categories (low, medium, and high speed) and direction into four categories. Table 4 and Figure 8 reveal the interesting results that, in the long-term time series, both Envisat and NSIDC data show for both regions a prominent mode of movement towards the north driven by strong winds from the RIS (for region-1, 65.62% and 57.08%, and for region-2, 45.89% and 57.58%, from Envisat and NSIDC data sets, respectively). The variability is clearly higher in the Envisat data set. Our results agree with the synoptic climatology developed by [43] for the Ross Sea and RIS based on the 10 m ERA Interim reanalysis data from 1979–2011. The northward RIS air stream (RAS) was found to be the dominant synoptic event impacting sea ice in the region. However, [43] also showed that the small-scale features were not resolved by this ERA Interim reanalysis data. The second dominating movement is towards the east due to the katabatic winds, which are also responsible for the opening of TNBP. As observed in Figure 8, the directional variability is lower in region-1 compared to region-2, which shows the contribution of winds from different directions likely driven by the katabatic winds from the Antarctic continent.

## 6. Conclusions

In this study, sea ice motion vectors from Envisat ASAR images were derived and compared with low-resolution NSIDC data in the highly dynamic and variable region of the Western Ross Sea region. There is a lack of sea ice drift information at high spatial resolution in this area, and this study addresses this gap and emphasizes the importance of high-resolution sea ice drift estimation for short-term analysis. We assessed the potential of high-resolution radar images for sea ice motion derivation and

provide an intrinsic reliability measure for the low-resolution product. For the detailed and synoptic comparisons of sea ice kinematics, we find COSI-Corr is a suitable tool to detect low-velocity sea ice drift. COSI-Corr has the potential to calculate large-scale deformational sea ice drift and rotation from consecutive high-resolution Envisat ASAR images. Envisat sea ice velocities were in good agreement in both magnitude and direction with manually drawn vectors and ECCC vector fields. Based on high correlation/visual analysis, we can conclude that the algorithm is appropriate for sea ice motion vector calculation over Antarctic sea ice. COSI-Corr is freely available for scientific use and is a user-friendly software, but it requires a commercial ENVI software license. It is convenient to use without prior knowledge of any programming language. It is computationally efficient and results are easy to visualize.

We also compared the Envisat sea ice velocities with lower spatial resolution NSIDC sea ice velocities. We showed that the low-resolution data lack a true representation of direction despite the high correlation in speed or vice versa. The highly dynamic nature of sea ice in the Ross Sea region is not fully represented in the low-resolution NSIDC data set. The averaging over areas with heterogeneous sea ice motion may underestimate the sea ice velocity since the direction changes so quickly within the area of interest. Also, the varying acquisition times of different products make it difficult to compare the sea ice drift because of short term variations. Furthermore, mixed land and sea ice pixels in coastal regions do not allow a meaningful assessment of sea ice drift in these regions. For the estimation of sea ice velocity, it is, therefore, necessary to consider the spatial and temporal resolution of satellite sensors, otherwise, the results might not show the actual drift of sea ice in the region of interest. However, low-resolution data have the ability to find long-term and broad-scale drift patterns. As the motion vectors show the displacement between two images despite the deviation in between the acquisitions, any in-between variation is unknown between an image pair. Therefore, further investigation is needed to correlate the sea ice motion vectors with winds and ocean currents to find out the effect of responsible dynamical forces. Also, the upcoming SAR satellites, e.g., NASA-ISRO SAR Mission (NISAR) together with Sentinel-1 (A and B), will provide better coverage of Antarctica and will improve the quality of sea ice estimates.

**Author Contributions:** U.F. has designed and developed the method, processed, analysed and validated all the data used in this study. S.H. processed the Envisat data at ECCC. The text is written by U.F. All the authors provided useful comments and suggestions to improve the paper. All authors have read and agree to the published version of the manuscript.

**Funding:** The research is supported by the University of Canterbury doctoral scholarship. U.F., W.R., and A.M. were partially supported by the Deep South National Science Challenge, New Zealand.

**Acknowledgments:** The author is like to thanks the COSI-Corr team for providing the software. The author is also thankful to Ori Ganoni for useful discussion on python programming and to the colleagues at Gateway Antarctica for the useful suggestions. The Envisat data is received within the ESA research project 30877 titled “Sea ice dynamics in the area of the Ross Sea Polynya” (PI W. Rack). NSIDC data is freely available and downloaded from <https://nsidc.org/data/nsidc-0116>.

**Conflicts of Interest:** The authors declare no conflict of interest.

## References

1. Bintanja, R.; Van Oldenborgh, G.; Drijfhout, S.; Wouters, B.; Katsman, C. Important role for ocean warming and increased ice-shelf melt in Antarctic sea-ice expansion. *Nat. Geosci.* **2013**, *6*, 376–379. [[CrossRef](#)]
2. Haas, C. Dynamics versus thermodynamics: The sea ice thickness distribution. *Sea Ice* **2010**, *82*, 113–152.
3. Leppäranta, M. *The Drift of Sea Ice*; Springer Science & Business Media: Heidelberg, Germany, 2011.
4. Lindsay, R.; Zhang, J. The thinning of Arctic sea ice, 1988–2003: Have we passed a tipping point? *J. Clim.* **2005**, *18*, 4879–4894. [[CrossRef](#)]
5. Parkinson, C.L. A 40-y record reveals gradual Antarctic sea ice increases followed by decreases at rates far exceeding the rates seen in the Arctic. *Proc. Natl. Acad. Sci. USA* **2019**, *116*, 14414–14423. [[CrossRef](#)]
6. Maqueda, M.; Willmott, A.; Biggs, N. Polynya dynamics: A review of observations and modeling. *Rev. Geophys.* **2004**, *42*. [[CrossRef](#)]

7. Dale, E.R.; McDonald, A.J.; Coggins, J.H.; Rack, W. Atmospheric forcing of sea ice anomalies in the Ross Sea polynya region. *Cryosphere* **2017**, *11*, 267–280. [[CrossRef](#)]
8. Coggins, J.H.; McDonald, A.J. The influence of the Amundsen Sea Low on the winds in the Ross Sea and surroundings: Insights from a synoptic climatology. *J. Geophys. Res. Atmos.* **2015**, *120*, 2167–2189. [[CrossRef](#)]
9. Kilifarska, N.; Bakmutov, V.; Melnyk, G. Geomagnetic influence on Antarctic climate—Evidences and mechanism. *Int. Rev. Phys.* **2013**, *7*, 242–252.
10. Haumann, F.A.; Gruber, N.; Münnich, M.; Frenger, I.; Kern, S. Sea-ice transport driving Southern Ocean salinity and its recent trends. *Nature* **2016**, *537*, 89–92. [[CrossRef](#)] [[PubMed](#)]
11. Sun, Y. Automatic ice motion retrieval from ERS-1 SAR images using the optical flow method. *Int. J. Remote Sens.* **1996**, *17*, 2059–2087. [[CrossRef](#)]
12. Petrou, Z.I.; Tian, Y. High-resolution sea ice motion estimation with optical flow using satellite spectroradiometer data. *IEEE Trans. Geosci. Remote Sens.* **2016**, *55*, 1339–1350. [[CrossRef](#)]
13. Fily, M.; Rothrock, D. Sea ice tracking by nested correlations. *IEEE Trans. Geosci. Remote Sens.* **1987**, *GE-25*, 570–580. [[CrossRef](#)]
14. Hall, R.; Rothrock, D. Sea ice displacement from Seasat synthetic aperture radar. *J. Geophys. Res. Oceans* **1981**, *86*, 11078–11082. [[CrossRef](#)]
15. Kwok, R. The RADARSAT geophysical processor system. In *Analysis of SAR Data of the Polar Oceans*; Springer: Berlin/Heidelberg, Germany, 1998; pp. 235–257.
16. Kwok, R.; Curlander, J.C.; McConnell, R.; Pang, S.S. An ice-motion tracking system at the Alaska SAR facility. *IEEE J. Ocean. Eng.* **1990**, *15*, 44–54. [[CrossRef](#)]
17. Thomas, M.; Geiger, C.; Kambhamettu, C. High resolution (400 m) motion characterization of sea ice using ERS-1 SAR imagery. *Cold Reg. Sci. Technol.* **2008**, *52*, 207–223. [[CrossRef](#)]
18. Hollands, T.; Dierking, W. Performance of a multiscale correlation algorithm for the estimation of sea-ice drift from SAR images: Initial results. *Ann. Glaciol.* **2011**, *52*, 311–317. [[CrossRef](#)]
19. Thomas, M.; Kambhamettu, C.; Geiger, C.A. Motion tracking of discontinuous sea ice. *IEEE Trans. Geosci. Remote Sens.* **2011**, *49*, 5064–5079. [[CrossRef](#)]
20. Komarov, A.S.; Barber, D.G. Sea ice motion tracking from sequential dual-polarization RADARSAT-2 images. *IEEE Trans. Geosci. Remote Sens.* **2014**, *52*, 121–136. [[CrossRef](#)]
21. Berg, A.; Eriksson, L.E. Investigation of a hybrid algorithm for sea ice drift measurements using synthetic aperture radar images. *IEEE Trans. Geosci. Remote Sens.* **2013**, *52*, 5023–5033. [[CrossRef](#)]
22. Muckenhuber, S.; Korosov, A.A.; Sandven, S. Open-source feature-tracking algorithm for sea ice drift retrieval from Sentinel-1 SAR imagery. *Cryosphere* **2016**, *10*, 913–925. [[CrossRef](#)]
23. Muckenhuber, S.; Sandven, S. Open-source sea ice drift algorithm for Sentinel-1 SAR imagery using a combination of feature tracking and pattern matching. *Cryosphere* **2017**, *11*, 1835. [[CrossRef](#)]
24. Korosov, A.A.; Rampal, P. A Combination of Feature Tracking and Pattern Matching with Optimal Parametrization for Sea Ice Drift Retrieval from SAR Data. *Remote Sens.* **2017**, *9*, 258. [[CrossRef](#)]
25. Giles, A.; Massom, R.; Heil, P.; Hyland, G. Semi-automated feature-tracking of East Antarctic sea ice from Envisat ASAR imagery. *Remote Sens. Environ.* **2011**, *115*, 2267–2276. [[CrossRef](#)]
26. Tschudi, M.A.; Meier, W.N.; Stewart, J.S. An enhancement to sea ice motion and age products. *Cryosphere Discuss* **2019**. [[CrossRef](#)]
27. Sumata, H.; Lavergne, T.; Girard-Ardhuin, F.; Kimura, N.; Tschudi, M.A.; Kauker, F.; Karcher, M.; Gerdes, R. An intercomparison of Arctic ice drift products to deduce uncertainty estimates. *J. Geophys. Res. Oceans* **2014**, *119*, 4887–4921. [[CrossRef](#)]
28. Hwang, B. Inter-comparison of satellite sea ice motion with drifting buoy data. *Int. J. Remote Sens.* **2013**, *34*, 8741–8763. [[CrossRef](#)]
29. Sumata, H.; Kwok, R.; Gerdes, R.; Kauker, F.; Karcher, M. Uncertainty of Arctic summer ice drift assessed by high-resolution SAR data. *J. Geophys. Res. Oceans* **2015**, *120*, 5285–5301. [[CrossRef](#)]
30. Sumata, H.; Gerdes, R.; Kauker, F.; Karcher, M. Empirical error functions for monthly mean Arctic sea-ice drift. *J. Geophys. Res. Oceans* **2015**, *120*, 7450–7475. [[CrossRef](#)]
31. Szanyi, S.; Lukovich, J.V.; Barber, D.; Haller, G. Persistent artifacts in the NSIDC ice motion data set and their implications for analysis. *Geophys. Res. Lett.* **2016**, *43*, 10800–10807. [[CrossRef](#)]
32. Heil, P.; Fowler, C.; Maslanik, J.; Emery, W.; Allison, I. A comparison of East Antarctic sea-ice motion derived using drifting buoys and remote sensing. *Ann. Glaciol.* **2001**, *33*, 139–144. [[CrossRef](#)]

33. Schwegmann, S.; Haas, C.; Fowler, C.; Gerdes, R. A comparison of satellite-derived sea-ice motion with drifting-buoy data in the Weddell Sea, Antarctica. *Ann. Glaciol.* **2011**, *52*, 103–110. [[CrossRef](#)]
34. Leprince, S.; Barbot, S.; Ayoub, F.; Avouac, J.-P. Automatic and precise orthorectification, coregistration, and subpixel correlation of satellite images, application to ground deformation measurements. *IEEE Trans. Geosci. Remote Sens.* **2007**, *45*, 1529–1558. [[CrossRef](#)]
35. *Envisat ASAR Product Handbook (Issue 2.2), Chapter 2: ASAR Products and Algorithms*; European Space Agency: Paris, France, 2007.
36. Scherler, D.; Leprince, S.; Strecker, M.R. Glacier-surface velocities in alpine terrain from optical satellite imagery—Accuracy improvement and quality assessment. *Remote Sens. Environ.* **2008**, *112*, 3806–3819. [[CrossRef](#)]
37. Ayoub, F.; Leprince, S.; Keene, L. *User's Guide to COSI-CORR Co-Registration of Optically Sensed Images and Correlation*; California Institute of Technology: Pasadena, CA, USA, 2009; p. 38.
38. Howell, S.E.; Komarov, A.S.; Dabboor, M.; Montpetit, B.; Brady, M.; Scharien, R.K.; Mahmud, M.S.; Nandan, V.; Geldsetzer, T.; Yackel, J.J. Comparing L-and C-band synthetic aperture radar estimates of sea ice motion over different ice regimes. *Remote Sens. Environ.* **2018**, *204*, 380–391. [[CrossRef](#)]
39. Howell, S.E.; Wohleben, T.; Dabboor, M.; Derksen, C.; Komarov, A.; Pizzolato, L. Recent changes in the exchange of sea ice between the Arctic Ocean and the Canadian Arctic Archipelago. *J. Geophys. Res. Oceans* **2013**, *118*, 3595–3607. [[CrossRef](#)]
40. Kwok, R. Satellite remote sensing of sea-ice thickness and kinematics: A review. *J. Glaciol.* **2010**, *56*, 1129–1140. [[CrossRef](#)]
41. Hollands, T.; Dierking, W. Dynamics of the Terra Nova Bay Polynya: The potential of multi-sensor satellite observations. *Remote Sens. Environ.* **2016**, *187*, 30–48. [[CrossRef](#)]
42. Hollands, T.; Linow, S.; Dierking, W. Reliability measures for sea ice motion retrieval from synthetic aperture radar images. *IEEE J. Sel. Top. Appl. Earth Obs. Remote Sens.* **2014**, *8*, 67–75. [[CrossRef](#)]
43. Coggins, J.H.; McDonald, A.J.; Jolly, B. Synoptic climatology of the Ross Ice Shelf and Ross Sea region of Antarctica: K-means clustering and validation. *Int. J. Climatol.* **2014**, *34*, 2330–2348. [[CrossRef](#)]



© 2020 by the authors. Licensee MDPI, Basel, Switzerland. This article is an open access article distributed under the terms and conditions of the Creative Commons Attribution (CC BY) license (<http://creativecommons.org/licenses/by/4.0/>).